Model-Simulated Influences of Shelterbelt Shape on Wind-Sheltering Efficiency

HAO WANG AND E. S. TAKLE

Department of Geological and Atmospheric Sciences and Department of Agronomy, Iowa State University, Ames, Iowa

(Manuscript received 6 November 1995, in final form 8 November 1996)

ABSTRACT

The authors report results of a numerical model used to simulate wind and turbulence fields for porous, living shelterbelts with seven different cross-sectional shapes. The simulations are consistent with results of Woodruff and Zingg whose wind-tunnel study demonstrated that all shelterbelts with very different shapes have nearly identical reduction of wind and turbulence. The simulations also showed that the pressure-loss (resistance) coefficient for smooth-shaped or streamlined shelterbelts is significantly smaller than that for rectangle-shaped or triangle-shaped shelterbelts with a windward vertical side. However, the shelter effects are not proportional to the pressure-loss coefficient (drag). Analysis of the momentum budget demonstrated that in the near lee and in the far lee, both vertical advection and pressure gradient have opposite roles in the recovery of wind speed. This behavior, combined with differences in permeability, is the likely cause of reduced sensitivity of shelter effects to shelterbelt shape.

1. Introduction

Shelterbelts and windbreaks are used throughout the world to improve surface climate and soil conditions for human and animal life and crop growth. Recently, large-scale agroecosystems consisting of shelterbelts have been established for environmental sustainability. The main effect of shelterbelts and windbreaks is to reduce surface wind speed. The change in microclimate and soil climate, in crop growth, and in animal comfort is mostly a consequence of the reduced wind speed (van Eimern et al. 1964). In the past fifty years, intensive shelterbelt research has been conducted with the goal of finding the optimum shelterbelt structure that, with minimum loss of crop land and minimum planting and maintenance cost, yields the optimum shelter effects. Several review papers (e.g., van Eimern et al. 1964; Plate 1971; Loucks 1983; Alcorn and Dodd 1984; McNaughton 1988; Heisler and DeWalle 1988) summarize the current status of shelterbelt research. Shelterbelt structure can be characterized by a combination of the internal structure (i.e., porosity) and the external structure (i.e., shape). Intensive studies of shelterbelt porosity have concluded that medium-dense shelterbelts have maximum average wind speed reduction over the total distance influenced by the shelterbelt. However, the effect of shelterbelt shape is still unsolved. There are not any theoretical and numerical studies on this topic. Only a few experimental studies were conducted and the experimental results were controversial. Some investigators suggested that smooth-shaped or streamlined shelterbelts produce smaller wind reduction than vertical-sided shelterbelts because the resistance for smooth-shaped or streamlined shelterbelts is smaller (e.g., Caborn 1957, 1965; Jensen 1974). However, Woodruff and Zingg (1953) reported that their wind-tunnel results gave only small differences of wind reduction by shelterbelts with very different shapes. They studied many streamlined shapes except, unfortunately, the rectangle shape, which is now commonly suggested for maximum wind reduction. It is very difficult, if not impossible, to separate the effect of shelterbelt shape from the effect of shelterbelt density in either laboratory or field experiments. In the previous experiments, the differences in shelterbelt density contaminated the data, resulted in controversial experimental conclusions, and made the results unreliable. Numerical modeling provides us a tool to separate both effects and to evaluate the role of shelterbelt shape alone.

Research on the effects of shelterbelt shape have both theoretical and practical significance. Both external and internal structures are important parameters for shelterbelt design. In practice, different shrub and tree species and planting configurations are selected and combined to achieve an optimum density and an optimum shape. If the effect of shelterbelt shape on the shelter efficiency is small as Woodruff and Zingg (1953) suggested, more freedom may be given to the design of optimum shelterbelts. However, aeronautical studies of the effects on flow due to shape for solid obstacles show that smooth shapes or streamlined obstacles have significantly small-

Corresponding author address: Dr. Hao Wang, Dept. of Geological and Atmospheric Sciences, Iowa State University, 3010 Agronomy Hall, Ames, Iowa 50011.
E-mail: wanghao@iastate.edu

er influence on perturbation pressure and flow field (Hoerner 1965). Many investigators (e.g., Caborn 1957, 1965; Jensen 1974; Gandemer 1979) suggested that the effect of shelterbelt shape on shelter efficiency is important. But theoretical and numerical studies have not been extended to consider *porous shelterbelts* embedded in *the atmospheric turbulent boundary layer*.

We hypothesize that the effects of the shape for *porous* shelterbelts embedded *in turbulent boundary layer* are different from that for *solid* barriers *in free flow* and, therefore, the results from aeronautical studies of solid bodies are not applicable to agricultural shelterbelts. We use a nonhydrostatic turbulent boundary layer model to study the effects of shelterbelt shape. We report results for seven different shelterbelt shapes including a rectangle, three different triangles, and three different streamlined shapes. We also analyze the momentum budget and related variables, such as perturbed pressure and vertical velocity, to interpret the simulated results.

2. The model and numerical experiments

a. Description of the model

The model has been used successfully to simulate the effect of shelterbelt density on flow patterns and has been described in our previous papers (Wang and Takle 1995a–c; 1996a,b). Here, we describe only the aspects of the model most relevant to this paper. We use the Boussinesq approximation, the nonhydrostatic formulation, equations of motion, and incompressible atmospheric continuity equation and subject these equations to phase averaging (Wang and Takle 1995a). The spatial averaging length scale is small relative to length scales of mean variation but large relative to the element dimensions of shelterbelts. This averaging process produces surface integrals over the complex boundaries of the obstacles that add extra terms to the mean and turbulence equations (Wang and Takle 1995a). For simplicity, we consider the equations of motion for neutral stratification. A typical shelterbelt height of about 10 m is much less than the height of the atmospheric boundary layer, so the effect of Coriolis forces may be neglected. Shelterbelts are generally planted in rows perpendicular to the prevailing wind direction, and their length is at least one order larger than their height. Therefore, we can consider a 2D computational domain (vertical z and horizontal x along the wind perpendicular to the shelterbelt), for which the basic equations of motion and continuity equation may be expressed as

$$\frac{\partial u}{\partial t} = -\frac{1}{\rho_0}\frac{\partial p}{\partial x} - u\frac{\partial u}{\partial x} - w\frac{\partial u}{\partial z} - \frac{\partial \overline{u'^2}}{\partial x} - \frac{\partial \overline{u'w'}}{\partial z} - C_d A U u \tag{1}$$

$$\frac{\partial w}{\partial t} = -\frac{1}{\rho_0}\frac{\partial p}{\partial z} - u\frac{\partial w}{\partial x} - w\frac{\partial w}{\partial z} - \frac{\partial \overline{u'w'}}{\partial x} - \frac{\partial \overline{w'^2}}{\partial z} - C_d A U w \tag{2}$$

$$\frac{\partial u}{\partial x} + \frac{\partial w}{\partial z} = 0, \tag{3}$$

where U is total mean wind speed, u and w are horizontal and vertical components of mean wind, u' and w' are their perturbations, p is pressure and ρ_0 is air density, the last term is drag force per unit volume exerted by the obstacle elements, C_d is a local dynamic resistance coefficient of individual leaf related to tree species, and A is the leaf area density ($m^2\ m^{-3}$).

Equations (1) and (2) of mean motion include turbulent stress terms for which we must apply a boundary layer turbulence closure scheme. We tested the sensitivity to a hierarchy of second-order closure schemes proposed by Mellor and Yamada (Mellor and Yamada 1974, 1982; Yamada and Mellor 1975; Yamada 1982), which are widely used in atmospheric sciences. Our results of different turbulence closure schemes on the flow are consistent with Wilson's (1985) findings that the simulated results are insensitive to turbulence closure schemes. We select the simplified second-order turbulent closure scheme (Wang and Takle 1995c, 1996a), which Yamada (1982) used to model turbulent airflow in and above a forest canopy.

We use the finite-difference method to discretize these equations into a set of algebraic equations that constitute tridiagonal matrices, with forward differencing for the time terms, centered differencing for pressure terms, and upstream differencing for advection terms. The modified Crank–Nicholson scheme is used for the turbulent flux terms (Paegle et al. 1976). We use the alternating direction implicit (ADI) method to solve these equations in both vertical and horizontal directions.

We use the time-dependent model to obtain a stationary solution. When we developed this model, we first examined the changes of predicted values with time under stationary forcing by integrating the model out to 60 h from initial neutral profiles. The mean kinetic energy (MKE) and turbulent kinetic energy (TKE) reached their stationary values after about 2 h. We also found that the computational accuracy for dynamic pressure was the key condition for keeping the cumulative error small for long time integrations. When we use double precision for dynamic pressure and a successive convergence criterion of $10^{-4}\ m^2\ s^{-2}$, we controlled the model relative computational error to be less than 10^{-3} and produced reliable stationary solutions. When the differences of TKE and MKE between successive 1-h integrations were less than the control level (in this paper, 0.01%), the computed results were considered to be steady-state results.

The model computational domain surrounding the

shelterbelt of height H is from $31H$ upstream to $80H$ downstream of the shelterbelt in the streamwise direction and from the ground surface to $15H$ in the vertical direction. All observations and our calculated results show that the windward maximum distance of perturbed flow is about $10H$, so we set the upstream boundary at $31H$. Previous experimental results and our results showed that ''open'' top boundary conditions had negligible effects on the simulated results of the effective shelter region (Wang and Takle 1995b). We divide the domain into 151 levels in the vertical direction with a constant interval of $0.1H$ and 241 grid points in horizontal direction with intervals of $0.05H$ within the shelter and $0.5H$ outside the shelter. The test of sensitivity to horizontal and vertical intervals shows no obvious differences in the simulated results with finer meshes.

We first omit the shelterbelt, assume that the ground surface is horizontally homogeneous, and compute the initial wind profile with a 1D version of the model under a prescribed wind speed at the model top boundary. This profile is also used as an inflow lateral boundary condition. The initial vertical velocity w is set equal to zero. At the outflow boundary, the normal derivatives of all physical variables are set equal to zero, and at the lower boundary, a no-slip condition is imposed for wind.

We have used this model to study the effect of shelterbelt porosity (density) on flow (Wang and Takle 1995b). Compared with all available experimental data, we have demonstrated our model can reproduce the characteristics of recirculations and simulate flow in the windward wind-reduction zone, the leeward wind-reduction zone, and the speedup zone over the shelterbelts. Detailed comparison with measurements on medium-dense shelterbelts also showed that our model gave correct predictions of the leeward wind recovery rate and overspeeding above the shelter.

b. Design of experiments

Shelterbelts may be constructed by use of different species of shrubs and trees in various configurations to create a variety of cross-sectional shapes. Several different shapes as illustrated in Fig. 1 are used to demonstrate the influence of shelterbelt shape on shelter effects. The seven shapes may be divided into three profile categories: rectangular, triangular, and streamlined. We denote them as ''H,'' ''A,'' and ''S,'' respectively. The triangular and streamlined shapes can be further subdivided. The letter J is used to symbolize a vertical side on the leeward edge of the shelter, and its mirror image, ''L,'' denotes vertical sides on the windward side. Here, H represents vertical sides at both edges, and A denotes a shelter with symmetrically sloping sides. By considering the general shape profile (first symbol) and symmetry of windward and leeward shape (second symbol) separately, we create seven shapes represented by HH, AA, AL, AJ, SA, SL, and SJ, respectively, as shown in Fig. 1.

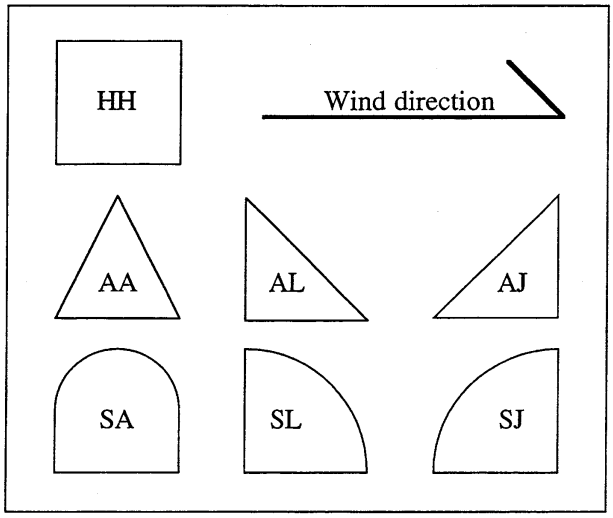

FIG. 1. Identifying labels for shelterbelt shapes used for simulations: (a) HH, (b) AA, (c) AL, (d) AJ, (e) SA, (f) SL, and (g) SJ.

We consider a shelterbelt of medium density because medium-dense shelterbelts have been found to have maximum sheltered distance in the leeward side and most shelterbelts and windbreaks in practice are built to be medium dense. According to Wilson (1985), the resistance coefficients k_r for natural shelterbelts may be approximated as

$$k_r = \int_{-\infty}^{\infty} C_d A \, dx, \tag{4}$$

where k_r is a dimensionless value, which describes the total density of shelterbelt. For shelterbelts with porosity of 50%, the corresponding k_r is 2.0 according to Hoerner's (1965) formula (Wilson 1985, 1987). To eliminate the effect of shelterbelt density on the simulated results, we set the total shelterbelt density $k_r = 2.0$ for all shelterbelts with different shapes (in practical application, we can input A directly and assign C_d value according to three species). Therefore, $A = k_r/C_d W_{SB}$, where W_{SB} is the width of shelterbelt, which is assigned according to the shape of shelterbelt in the model as shown in Fig. 1. Here, C_d is a local dynamic resistance coefficient related to the characteristics of individual leaf (Thom 1971; Mayhead 1973; Holland et al. 1991). Figure 2 shows the vertical profiles of leaf (surface) area density for different shapes. Here, k_r is different from drag coefficient, because drag is related not only to shelterbelt density, but also to squared wind speed inside the shelterbelt as revealed in Eqs. (1) and (2). Our calculated drag coefficients for different shapes are significantly different even for the same k_r (Table 3). We set the overall density $k_r = 2.0$ for all shelterbelts of different shapes to eliminate the effect of shelterbelt density on the simulated results. In contrast, it is very difficult to separate the effect of shelterbelt shape from the effect of shelterbelt density in either laboratory experiments

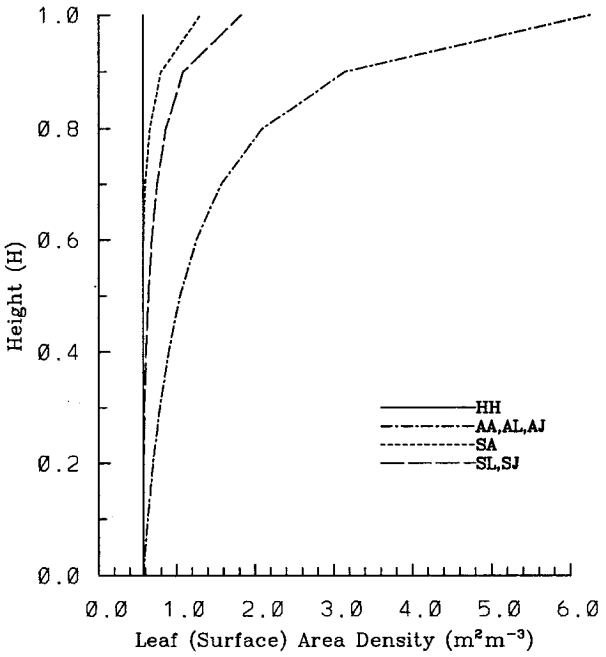

FIG. 2. Leaf area density for shelterbelts of different shapes used for simulations.

or field measurements, on which the previous controversial conclusions were based (e.g., Caborn 1957, 1965; Jensen 1974; Woodruff and Zingg 1953).

3. Results and discussion

The horizontal profile of wind speed from windward 10*H* to leeward 30*H* reveals the characteristics of wind reduction around the shelter as shown in Fig. 3. The shelter effect is most often represented by the shelter distance over which the shelterbelt reduces wind speed by a given significant percentage, commonly 80% (van Eimern et al. 1964; Heisler and DeWalle 1988). The minimum wind speed, that is, maximum wind reduction, and its location also can be used as indicators of the shelter effect (Wilson 1985; Heisler and DeWalle 1988). The locations of the minimum wind speed are $x = 5H$ at $z = 0.5H$ (Fig. 3a), $x = 7H$ at $z = 0.3$ (figure omitted), and $x = 9H$ at $z = 0.1H$ (figure omitted), which are consistent with the observations that show the minimum closer to the shelter for higher z values (van Eimern et al. 1964; Heisler and DeWalle 1988). The minimum relative wind speeds for the rectangle-shaped shelterbelt are 30% at $z = 0.5H$ (Fig. 3a), 26% at $z = 0.4H$, 20% at $z = 0.3H$, which are also in agreement with the simulation of Wilson (1985) and measurements at $z = 0.38H$ of Bradley and Mulhearn (1983) and Finnigan and Bradley (1983) as well as other data as summarized in the review papers of van Eimern et al. (1964) and Heisler and DeWalle (1988). The shelter distances (d_{p80}) within which the wind speed was reduced by at least 20% are 18*H* at $z = 0.5H$, 20*H* at $z = 0.3H$ (figure omitted), 22*H* at $z = 0.1H$, and 16.5*H* at $z = 0.7H$, which also compare well with available data.

We were surprised to find that although the shapes of shelterbelts are very different and drag forces for different shapes are also significantly different (Table 3), as shown in Fig. 3, there are only small differences in wind speed reduction by shelterbelts of different shapes, even in the region of maximum wind reduction. The effect of shelterbelt shape on the shelter distance is neg-

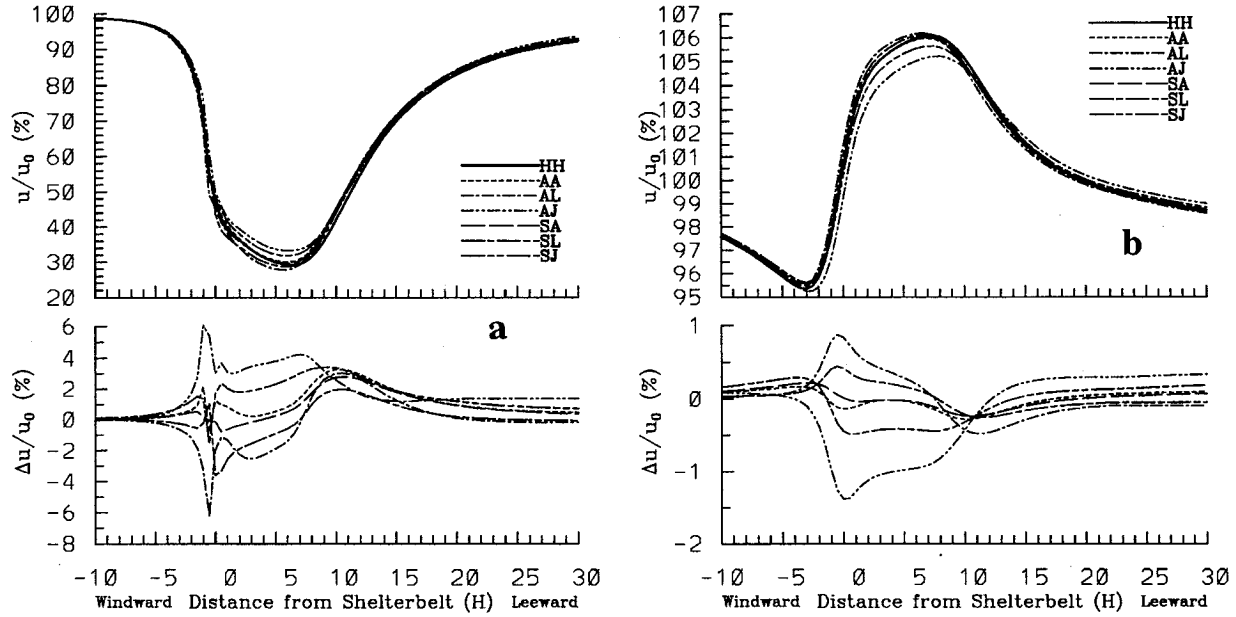

FIG. 3. Wind speed produced by various shelter shapes, normalized by the upstream undisturbed wind speed, at different levels: (a) $z = 0.5H$ and (b) $z = 3.0H$. The bottom plots show the differences in wind speed from that for HH.

TABLE 1. Effect of shelterbelt shape on mean shelter efficiency E_{30} (%) over a leeward distance of 30H lee at various heights.

Shape	HH	AA	AL	AJ	SA	SL	SJ
$z = 0.1H$	49.0	48.2	50.5	45.2	47.9	49.2	46.9
$z = 0.3H$	42.9	41.9	43.5	40.1	41.9	42.9	41.0
$z = 0.5H$	36.7	35.4	36.5	34.6	35.7	36.6	34.9
$z = 0.7H$	31.1	29.5	30.3	29.3	30.0	30.6	29.2
$z = 1.0H$	21.6	19.7	20.6	19.6	20.0	20.6	19.5

ligible. Slightly larger differences in wind speed reduction by shelterbelts of different shapes exist in the near lee (0–10H) where the maximum wind reduction is located. The largest differences of the maximum wind reduction for shelterbelts with different shapes are 6% at $z = 0.5H$ (Fig. 3a), 6.5% at $z = 0.3H$ (figure omitted), 9% at $z = 0.1H$ (figure omitted), and 4% at $z = 0.7H$ (figure omitted). We anticipated that there would be a large effect of the shape near and above the shelterbelt top. However, for the level of $z = 1.0H$, the maximum difference in wind speed for different shapes is only about 6%, even though the wind reduction is as large as 50%. At $z = 1.5H$ where the wind reduction is very small, differences of only 3% are simulated for different shapes. The effect of shelterbelt shape on speedup of wind over the shelter is shown in Fig. 3b for $z = 3H$. The maximum difference in wind speed among different shapes is only about 2% although the maximum speedup also is small.

Konstantinov's (1966) effectiveness index (E_{30}), defined as the average wind reduction over 30H in the lee was used as a descriptor of the shelter effect. We calculate E_{30} from horizontal profiles of wind at different levels for different shelterbelt shapes (see Table 1). Here, E_{30} decreases with increasing height, and the calculated E_{30} is consistent with previous measurements as summarized by van Eimern et al. (1964) and Heisler and DeWalle (1988). From Table 1, we can see that the differences in E_{30} for different shelterbelt shapes are very small.

The shelterbelts with windward vertical sides cause the maximum wind reduction at lower levels (Fig. 3). However, at higher levels—for example, $z = 0.7H$ and 1.0H—shape HH produces the maximum wind reduction, and above the canopy level AL produces the maximum and AJ produces the minimum increase in wind as shown in Fig. 3b.

Permeability is defined as percentage of upwind mass flux below the top of the shelter at height that passes through the shelter. Incompressibility of the wind field allows us to express this as percentage of wind speed immediately behind the shelter over upstream undisturbed wind speed. For porous shelterbelts, the permeability is of interest because its departure from 100% indicates the mass flux that must be replaced as the wind field recovers to the undisturbed equilibrium in the lee. We calculate the mean permeability over the shelterbelt height for different shelterbelt shapes and list them in Table 2. The maximum difference in permeability among seven different shapes is only 7.6%, with AL having the maximum permeability and AJ having the minimum permeability. The shelterbelts with windward vertical sides (HH, AL, and SL) have larger permeability, whereas the shelterbelts with windward slope sides (AJ, SJ, AA, and SA) have smaller permeability, because airflow more easily passes over shelterbelts with windward sloped sides than over shelterbelts with windward vertical sides.

TABLE 2. Effect of shelterbelt shape on mean permeability.

Shape	HH	AA	AL	AJ	SA	SL	SJ
Permeability (%)	49.4	48.1	52.0	44.4	48.8	49.6	47.8

The effect of shelterbelt shape on TKE is also small (as shown in Fig. 4). The simulated TKE at $z = 0.5H$ (Fig. 4b) shows that shelterbelts decrease TKE in the near lee (0–8H) to a maximum decrease of 60% at 3.5H and increase TKE in the middle and far lee with a maximum increase of 60% at 11.5H, which is in agreement with available data as summarized by McNaughton (1988). The maximum differences in TKE for shelterbelts with different shapes are 5% at $x = 3.5H$ and 8% at $x = 11.5H$, which occur near the locations of the two extreme values of TKE horizontal profiles. However, from Figs. 4a and 4b, we can see horizontal displacements of the curves—for example, the curve for the AJ moves a little downstream—and the curve for AL moves a little upstream. Displacements of the curves are rather small, so if field measurements are made only at a few points downwind of the shelter, differences in TKE as large as 40% may be observed for different shelterbelt shapes. Near the ground, all shelter shapes reduced TKE over a longer leeward distance (29H) as shown in Fig. 4a. Near and above the shelterbelt top, TKE increases over the entire lee, and the maximum TKE at $z = 1H$ is as large as three times the upstream undisturbed TKE_0 as shown in Fig. 4c. Near the shelterbelt top, shelterbelt shape has a significant effect on TKE, with differences as large as 70% at $z = 1H$. Shapes AL and SL cause maximum increases, and AJ and SJ cause minimum increases in TKE (Fig. 4c).

We plot horizontal profiles of vertical turbulent flux in Fig. 5, where $u'w'$ has been normalized by the undisturbed turbulent flux. The effect of the shelterbelt on turbulent flux generally is similar to its effect on TKE, and the effect of shelterbelt shape also is quite small. Only near the shelterbelt top does shelterbelt shape have a significant effect on turbulent flux. Differences in vertical velocity due to shelter shape are also small, except near the shelter top as shown in Fig. 6.

Shelterbelt shape significantly affects the perturbed pressure around the shelter, as shown in Figs. 7a–c, which show the simulated static pressure perturbation normalized by the upwind mean kinetic energy (MKE) at the height of shelterbelt top for levels of $z = 0.5H$,

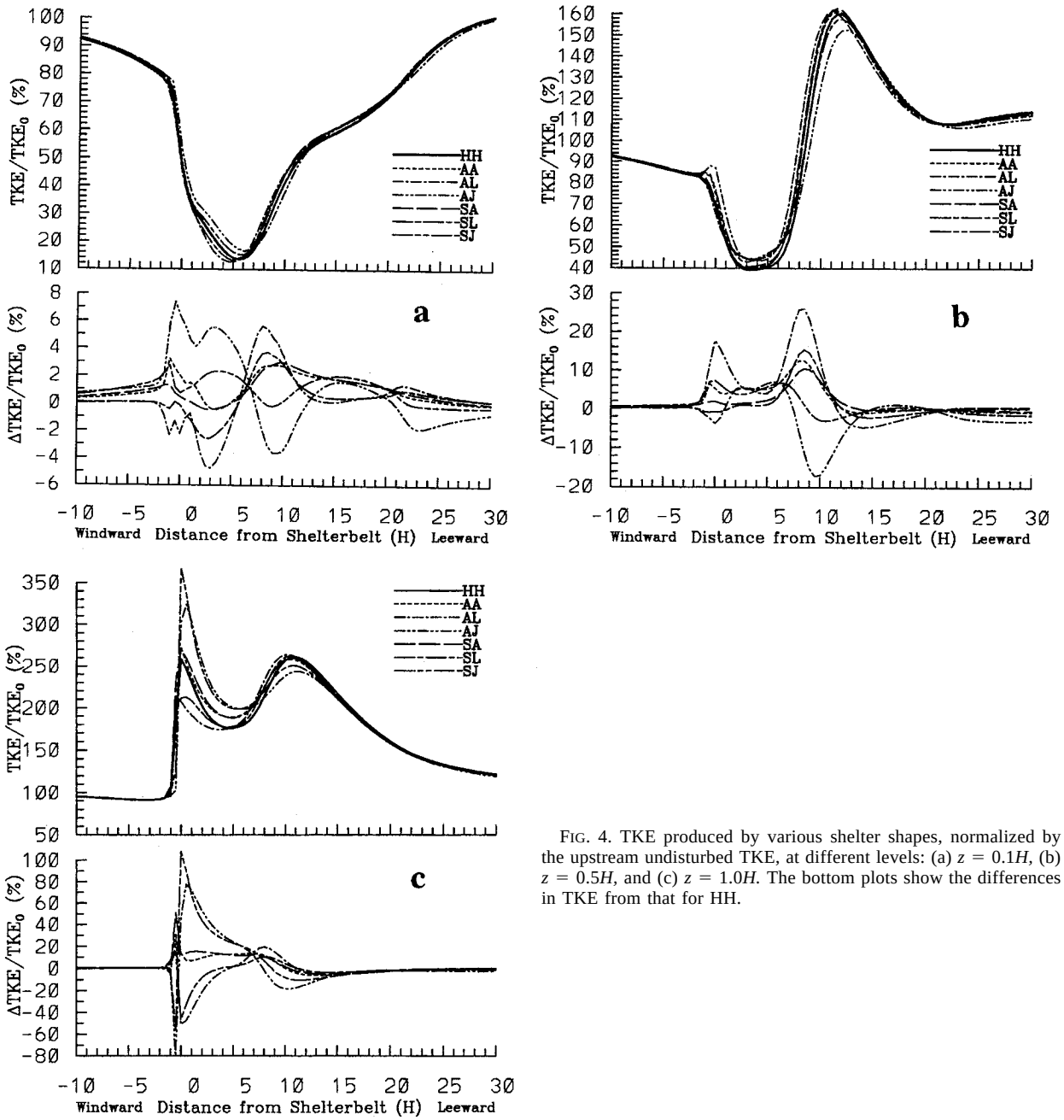

FIG. 4. TKE produced by various shelter shapes, normalized by the upstream undisturbed TKE, at different levels: (a) $z = 0.1H$, (b) $z = 0.5H$, and (c) $z = 1.0H$. The bottom plots show the differences in TKE from that for HH.

1*H*, and 3*H*, respectively. Pressure increases as air approaches the belt, with the AL shape causing the most rapid increase in the pressure and smooth-shaped shelterbelts causing smaller perturbations (Fig. 7a). All shelters produce an abrupt decrease of pressure across the belt, with AL producing the maximum drop. In the lee, the perturbed pressure gradually recovers to its equilibrium undisturbed value. The recovery rate is very small, and a perturbed pressure plateau forms in the near lee (1*H*–7*H*) (Fig. 7a). The pressure perturbation slightly increases from the ground to the shelterbelt top, but decreases with further increase of height (Figs. 7a–c). From Fig. 7a, we also can see that although the maximum perturbed pressure is only 62% on the windward side and 35% on the leeward side, differences in the perturbed pressure for different shelterbelt shapes are as large as 30% windward and 20% leeward. The effect of shelterbelt shape on pressure perturbation increases with increasing height as shown in Figs. 7b and 7c.

The pressure-loss coefficient or resistance coefficient (C_p), which is defined as mean pressure drop across an obstacle normalized by dynamic pressure or MKE of

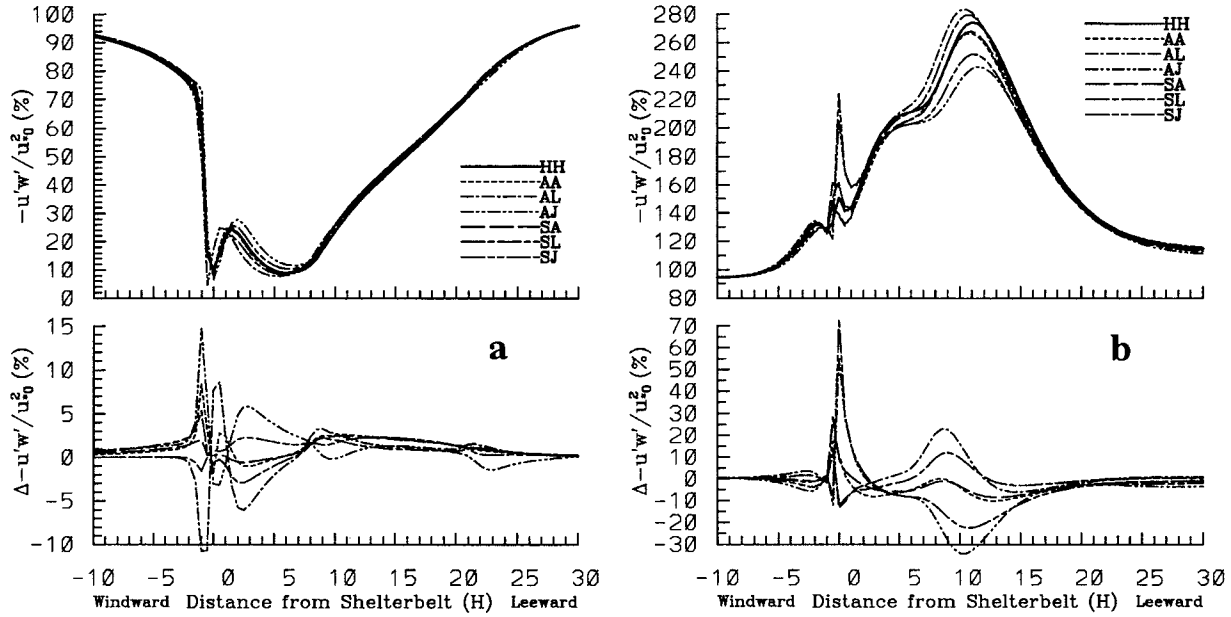

FIG. 5. Turbulent stress, normalized by the upstream undisturbed turbulent stress, for various shelter shapes at different levels: (a) $z = 0.1H$ and (b) $z = 3.0H$. The bottom plots show the differences in turbulent stress from that for HH.

the undisturbed flow at the height of the top of the obstacle, is often used to characterize the aerodynamics of obstacles (Hoerner 1965). It is the total drag of the shelterbelt. As shown in Table 3, the pressure-loss coefficient is strongly dependent on shelterbelt shape, as anticipated. The triangle-shaped shelterbelt with a windward vertical side (AL) has a 33% larger C_p than the smooth-shaped shelterbelts. Our calculated results are consistent with aerodynamic measurements for solid obstacles, which were summarized by Hoerner (1965) as follows: $C_d = 1.00$, 1.03, 1.28, 1.2, and 0.8 for solid shapes AA, AJ, AL, HH, and SA, respectively. It would seem reasonable to infer from pressure-loss coefficients, as many previous investigators have, that shelterbelt shape significantly affects shelter efficiency and that smooth-shaped or streamlined shelterbelts significantly reduce the shelter efficiency. However, as demonstrated in our analysis of numerical simulations and Woodruff and Zingg's (1953) measurements (summarized by Heisler and DeWalle 1988), shelter efficiency is affected very little by shelterbelt shape. An analysis of the momentum budget for different shelterbelt shapes will clarify this apparent discrepancy.

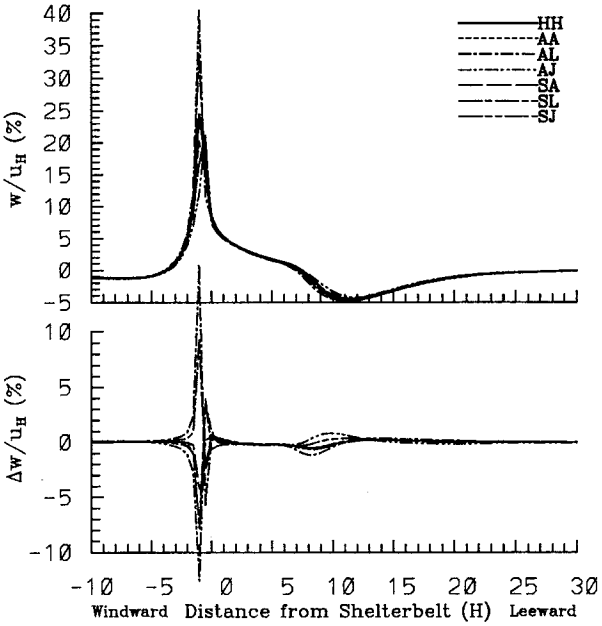

FIG. 6. Vertical velocity at $z = 1.1H$, normalized by the upstream undisturbed wind speed at the height of the shelterbelt top, for various shelter shapes. The bottom plots show the differences in vertical velocity from that for HH.

From Eq. (1), we know that the acceleration of the wind in the lee is determined by horizontal advection, vertical advection, turbulent transport (terms 4 and 5 on rhs of the equation), and pressure gradient, horizontal profiles of which are shown in Fig. 8. Terms of Eq. (1) have been normalized by H/MKE_H and become dimensionless acceleration in Fig. 8. Horizontal advection, which is determined by horizontal profile of mean wind, causes acceleration upstream of the minimum wind ($6H$ leeward) and deceleration beyond that point. Shelterbelt shape has little effect on this term (Fig. 8a). Vertical advection, shown in Fig. 8b, is determined by both vertical gradient of wind and vertical velocity and causes deceleration in the near lee (0–$8H$) and acceleration in the middle lee ($9H$–$25H$). Although the differences in

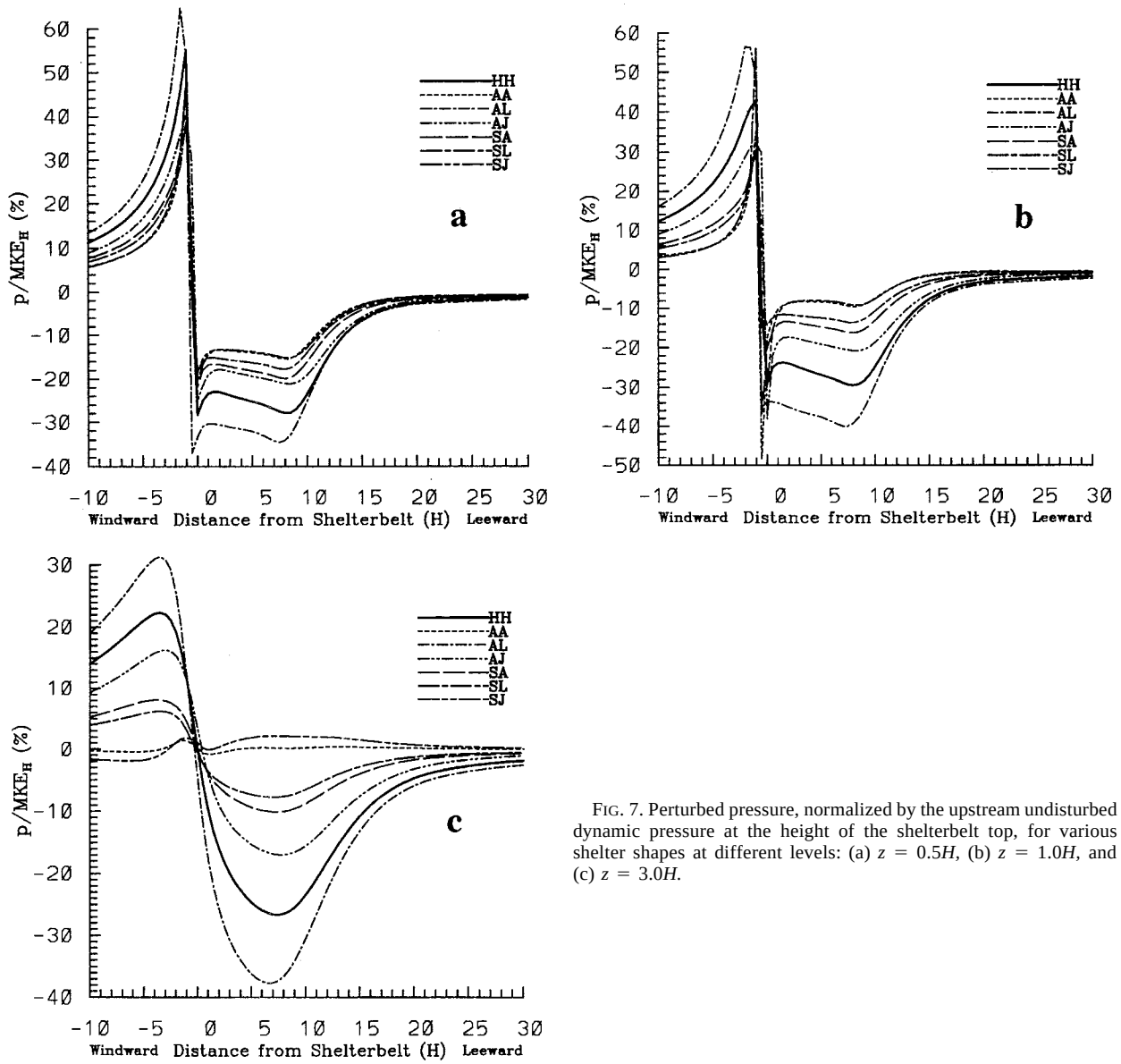

FIG. 7. Perturbed pressure, normalized by the upstream undisturbed dynamic pressure at the height of the shelterbelt top, for various shelter shapes at different levels: (a) $z = 0.5H$, (b) $z = 1.0H$, and (c) $z = 3.0H$.

vertical velocity for different shapes are small, different vertical gradients of wind create differences in vertical advection of momentum. Turbulent transport of momentum generally causes the recovery (acceleration) of wind, except immediately behind the shelter (0–3*H*) and in the middle lee (25*H*–35*H*), where it may cause deceleration because of the vertical variation of turbulence intensity. Among the different shelterbelt shapes, AL has largest turbulent transport from 0 to 10*H* leeward and smallest turbulent transport from 10*H* to 20*H* (Fig. 8c). The pressure gradient (Fig. 8d) causes deceleration immediately behind the shelter (0–2*H*), acceleration in the near lee (2*H*–8*H*), and deceleration in the middle lee (8*H*–23*H*). From Fig. 8a, we can see that HH and AL may cause larger acceleration in the near lee and largest deceleration in the middle lee, but this deceleration more rapidly decreases in the range of 11*H*–23*H* leeward.

TABLE 3. Effect of shelterbelt shape on pressure-loss coefficient C_p.

Shape	HH	AA	AL	AJ	SA	SL	SJ
C_p	0.782	0.633	0.843	0.658	0.637	0.640	0.644

Porous shelterbelts allow airflow to pass through, which leads to deceleration on the leeward side giving a minimum wind speed a few *H* from the belt (Fig. 3a). The interaction between airflow and pressure causes the pressure plateau in the near lee (Fig. 7), which produces both positive and negative acceleration on the leeward

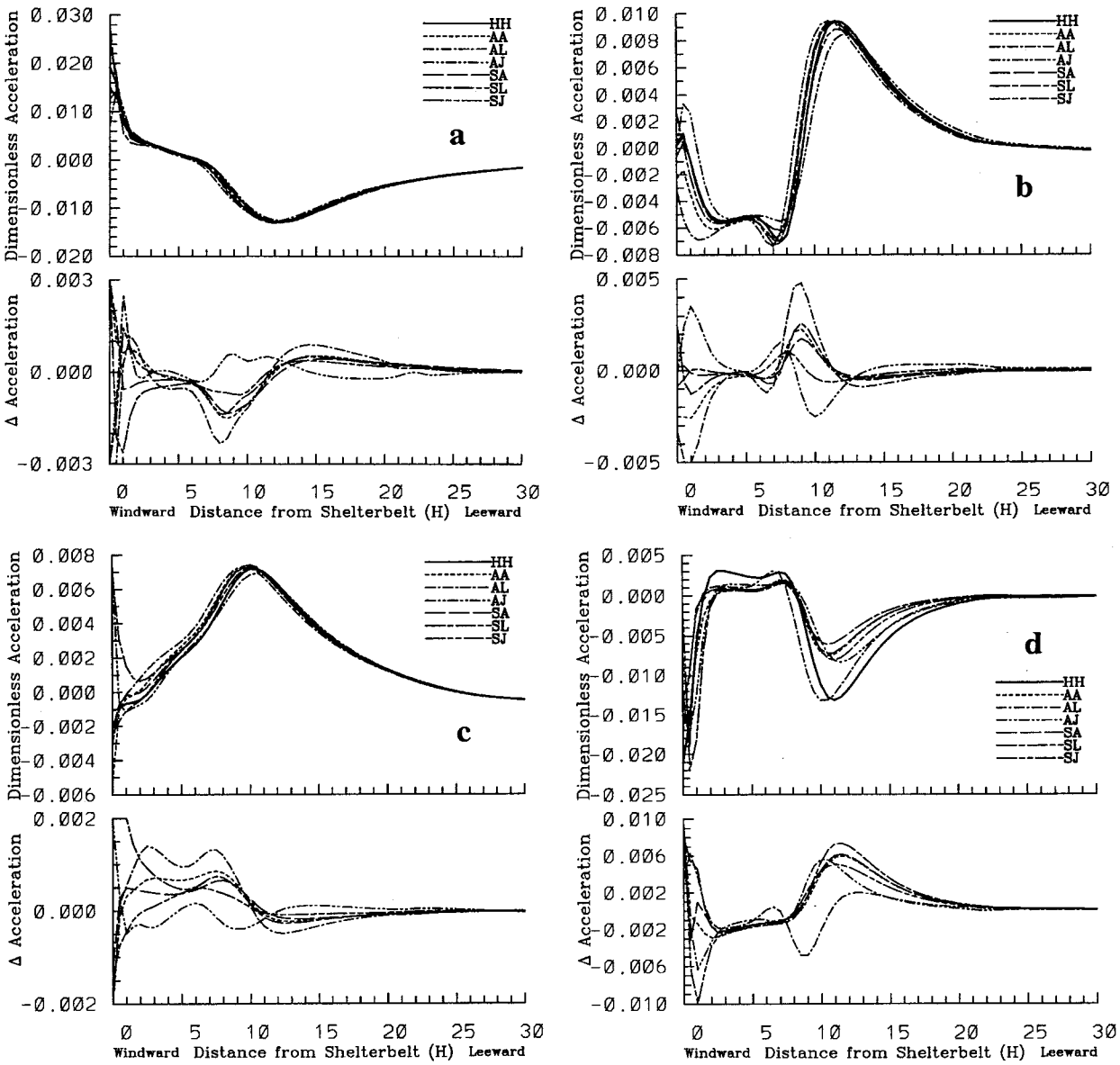

FIG. 8. Horizontal profiles of dimensionless acceleration at $z = 0.5H$ for shelterbelts with different shapes: (a) horizontal advection, (b) vertical advection, (c) turbulent transport, and (d) pressure gradient. The bottom plots show the differences from that for HH.

side (as shown in Fig. 8d). Although HH and AL have largest drag and deceleration, they cause the largest acceleration in the near lee (1*H*–9*H*). In contrast, shelterbelts having other shapes (e.g., SL) have smaller drag and deceleration, but they also cause smaller acceleration in the near lee. Therefore, the presence of both positive and negative pressure gradients on the leeward side reduces the sensitivity of sheltering efficiency to shelterbelt shape and minimizes the total effect of shelterbelt shape. Deceleration of air that passes through the shelter causes upward motion in the lee, which extends the ascending motion that begins windward to 9*H* leeward from the shelter. Ascending motion brings air with low momentum to higher levels and causes deceleration. Comparing Fig. 8b with 8d, we can see that the effects of vertical advection and perturbation pressure gradient on the recovery of wind are opposite in the near and middle lees, which may reduce the effect of shelterbelt shape. In addition, the larger permeability for shelterbelt shapes with larger resistance (AL and HH, Tables 2 and 3) also leads to the insensitivity of the shelter effect to shelterbelt shape, because larger resistance may cause larger deceleration in the mid lee (Fig. 8d).

4. Summary

We used a nonhydrostatic boundary layer turbulence model to test the sensitivity of shelter effects to shelter

shape for seven different shapes. The simulated results are in agreement with measurements of Woodruff and Zingg (1953) that the differences in the shelter effects for shelterbelts with different shapes are small and negligible.

The simulations also demonstrated that shelterbelt shape significantly affects perturbed pressure field and that the pressure-loss coefficient is a function of shelterbelt shape. Smooth-shaped or streamlined shelterbelts have significantly smaller pressure-loss coefficients than shelterbelts that are either rectangle shaped with both vertical sides or triangle shaped with the windward side vertical. The simulated dependence of pressure-loss coefficient on shape is consistent with aeronautical measurements for solid obstacles. However, we concluded that we cannot infer shelter effects of porous shelterbelts based on the pressure-loss coefficient alone. The resistance coefficient or pressure-loss coefficient commonly used is not a good descriptor of the shelter efficiency of shelterbelts. The penetrating airflow and its interaction with pressure extend the zone of upward motion far behind the shelter and cause a pressure plateau in the near lee. Analysis of the momentum budget demonstrated that both pressure gradient and vertical advection have opposite roles in the near lee and in the middle lee in the recovery of wind speed, which possibly reduces the effect of shelterbelt shape.

Acknowledgments. The authors thank three anonymous reviewers for their helpful and constructive comments. This research was supported by USDA/CSRS NRI Competitive Grant 93371018954 and USDOE/NIGEC Grant DE-FC 0390ER61010.

REFERENCES

Alcorn, K. L., and M. W. Dodd, 1984: *Windbreaks for Conservation—An Annotated Bibliography.* California Department of Conservation, Division of Land Resource Protection, 145 pp.

Bradley, E. F., and P. S. Mulhearn, 1983: Development of velocity and shear stress distributions in the wake of a porous fence. *J. Wind Eng. Ind. Aerodyn.,* **15,** 145–156.

Caborn, J. M., 1957: Shelterbelts and microclimate. *For. Comm. Bull. (Edinburgh),* **29,** 1–129.

——, 1965: *Shelterbelts and Windbreaks.* Faber and Faber, 288 pp.

Finnigan, J. J., and E. F. Bradley, 1983: The turbulent kinetic energy budget behind a porous barrier: An analysis in streamline co-ordinates. *J. Wind Eng. Ind. Aerodyn.,* **15,** 157–168.

Gandemer, J., 1979: Wind shelters. *J. Ind. Aerodyn.,* **4,** 371–389.

Heisler, G. M., and D. R. Dewalle, 1988: Effects of windbreak structure on wind flow. *Agric. Ecosys. Environ.,* **22/23,** 41–69.

Hoerner, S. F., 1965: *Fluid Dynamic Drag.* Hartford House, 1–29.

Holland, M. R., J. Grace, and C. L. Hedley, 1991: Momentum absorption by dried-pea crops. Part II. Wind tunnel measurements of drag on isolated leaves and pods. *Agric. For. Meteor.,* **54,** 81–93.

Jensen, M., 1974: The aerodynamics of shelter. FAO/DEN/TF Rep. 123, 132–145. [Available from Food and Agricultural Organization of the United Nations, Rome, Italy.]

Konstantinov, A. R., 1966: *Evaporation in Nature.* National Science Foundation, 523 pp.

Loucks, W. L., 1983: Windbreak bibliography. Great Plains Agriculture Council Publ. 113, 111 pp. [Available from Forestry Committee, Great Plains Council, Lincoln, NE 68583.]

Mayhead, G. J., 1973: Some drag coefficients for British forest trees derived from wind tunnel studies. *Agric. Meteor.,* **12,** 123–130.

McNaughton, K. G., 1988: Effects of windbreaks on turbulent transport and microclimate. *Agric. Ecosys. Environ.,* **22/23,** 17–39.

Mellor, G. L., and T. Yamada, 1974: A hierarchy of turbulence closure models for planetary boundary layers. *J. Atmos. Sci.,* **31,** 1791–1806.

——, and ——, 1982: Development of a turbulent closure model for geophysical fluid problems. *Rev. Geophys. Space Sci.,* **20,** 851–875.

Paegle, J., W. G. Zdunkowski, and R. M. Welch, 1976: Implicit differencing of predictive equations of the boundary layer. *Mon. Wea. Rev.,* **104,** 1321–1324.

Plate, E. J., 1971: The aerodynamics of shelter belts. *Agric. Meteor.,* **8,** 203–222.

Thom, A. S., 1971: Momentum absorption by vegetation. *Quart. J. Roy. Meteor. Soc.,* **97,** 414–428.

van Eimern, J., R. Karschon, L. A. Razumova, and G. W. Robertson, 1964: Windbreaks and shelterbelts. World Meteorological Organization Tech. Note 59, 188 pp. [Available from World Meteor. Org., Publications Sales Unit, Case Postale 2300, CH-1211 Geneva 2, Switzerland.]

Wang, H., and E. S. Takle, 1995a: Boundary-layer flow and turbulence near porous obstacles. Part I: Derivation of a general equation set for a porous medium. *Bound.-Layer Meteor.,* **74,** 73–88.

——, and ——, 1995b: A numerical simulation of boundary-layer flows near shelterbelts. *Bound.-Layer Meteor.,* **75,** 141–172.

——, and ——, 1995c: Numerical simulations of shelterbelt effects on wind direction. *J. Appl. Meteor.,* **34,** 2206–2219.

——, and ——, 1996a: On three-dimensionality of shelterbelt structure and its influences on shelter effects. *Bound.-Layer Meteor.,* **79,** 83–105.

——, and ——, 1996b: On shelter efficiency of shelterbelts in oblique wind. *Agric. For. Meteor.,* **81,** 95–117.

Wilson, J. D., 1985: Numerical studies of flow through a windbreak. *J. Wind Eng. Ind. Aerodyn.,* **21,** 119–154.

——, 1987: On the choice of a windbreak porosity profile. *Bound.-Layer Meteor.,* **38,** 37–39.

Woodruff, N. P., and A. W. Zingg, 1953: Wind tunnel studies of shelterbelt models. *J. For.,* **53,** 173–178.

Yamada, T., 1982: A numerical model study of turbulent airflow in and above a forest canopy. *J. Meteor. Soc. Japan,* **60,** 438–454.

——, and G. L. Mellor, 1975: A simulation of the Wangara atmospheric boundary layer data. *J. Atmos. Sci.,* **32,** 2309–2329.